Journal of
Synchrotron
Radiation

ISSN 0909-0495

Received 21 June 2005
Accepted 22 November 2005

The PILATUS 1M detector

Ch. Broennimann,[a]* E. F. Eikenberry,[a] B. Henrich,[a] R. Horisberger,[a] G. Huelsen,[a] E. Pohl,[a] B. Schmitt,[a] C. Schulze-Briese,[a] M. Suzuki,[b] T. Tomizaki,[a] H. Toyokawa[b] and A. Wagner[a]

[a]Paul Scherrer Institute, CH-5232 Villigen, Switzerland, and [b]Japan Synchrotron Radiation Research Institute, 1-1-1 Kouto, Mikazuki-cho, Sayo-gun, Hyogo 679-5198, Japan.
E-mail: christian.broennimann@psi.ch

The PILATUS 1M detector is a hybrid pixel array detector with over one million pixels that operate in single photon counting mode. The detector, designed for macromolecular crystallography, is the largest pixel array detector currently in use at a synchrotron. It is a modular system consisting of 18 multichip modules covering an area of 21 cm × 24 cm. The design of the components as well as the manufacturing of the detector including the bump-bonding was performed at the Paul Scherrer Institute (PSI). The use of a single photon counting detector for protein crystallography requires detailed studies of the charge collection properties of the silicon sensor. The 18 modules are read out in parallel, leading to a full frame readout-time of 6.7 ms. This allows crystallographic data to be acquired in fine-φ-slicing mode with continuous rotation of the sample. The detector was tested in several experiments at the protein crystallography beamline X06SA at the Swiss Light Source at PSI. Data were collected both in conventional oscillation mode using the shutter, as well as in a fine-φ-slicing mode. After applying all the necessary corrections to data from a thaumatin crystal, the processing of the conventional data led to satisfactory merging R-factors of the order of 8.5%. This allows, for the first time, determination of a refined electron density map of a macromolecular biological crystal using a silicon pixel detector.

Keywords: hybrid pixel detector; single photon counting; macromolecular crystallography.

1. Introduction

X-ray crystallography is presently the most important method for determining molecular structures of proteins at atomic resolution. This technique has benefited greatly from the high flux and brightness of third-generation synchrotron sources, from recent software advances and from the development of large-area tiled CCD detectors. However, the latter have limitations with respect to readout speed, dynamic range, point-spread function and detective quantum efficiency. Hybrid pixel detectors, as developed for high-energy physics experiments, can overcome these deficiencies (see, for example, Gemme, 2003; Riedler *et al.*, 2003; Schnetzer, 2003).

A hybrid pixel detector is composed of a silicon sensor, which is a two-dimensional array of pn-diodes usually processed in high-resistivity silicon, connected to an array of readout channels designed with advanced CMOS technology. Each readout channel is connected to its corresponding detecting element through a microscopic metallic ball, usually with a diameter of 15–25 μm. This process is called flip-chip bump-bonding. The bump-bonding can be realised in different ways, for example with indium or with lead–tin solder bumps. The great advantage of this approach is that standard technologies can be used for the sensor and the readout electronics. Both of them can be optimized separately, as the best silicon substrates for X-ray detection and for high-speed/high-quality electronics are very different. Moreover, the small size of the pixel and of the interconnection results in a very low capacitance, usually of the order of 100 fF. This low capacitance has the beneficial effect of reducing the noise and power consumption of the pixel readout electronics.

X-ray data collection can be improved with detectors operating in single photon counting mode. A hybrid pixel which features single photon counting comprises a preamplifier, which amplifies the charge generated in the sensor by the incoming X-ray, and a discriminator, which produces a digital signal if the incoming charge exceeds a pre-defined threshold. The discriminator feeds a counter, which then leads to completely digital storage and readout of the number of detected X-rays per pixel. Several groups are developing

single photon counting detectors for different X-ray applications (Llopart *et al.*, 2002; Boudet *et al.*, 2003).

The most important features of hybrid pixel single photon counting detectors are the following:

(i) No dark current and no readout noise, resulting in maximum dynamic range.

(ii) An excellent point spread function of one pixel.

(iii) High quantum efficiency. At 8 keV the absorption of a 0.3 mm-thick Si sensor is almost 100% of the incoming radiation; at 12 keV 75% of the radiation is stopped.

(iv) Short readout time. Since the information is stored digitally, pixel detectors can be read out very quickly; readout times in the millisecond range are state of the art.

The PILATUS 1M detector [Pixel Apparatus for the Swiss Light Source (SLS)] is designed for the macromolecular crystallography beamline X06SA of the SLS, and is especially tailored to collect fine-φ-sliced crystallographic data at high speed in the continuous sample rotation mode. This method is described in more detail by Broennimann *et al.* (2003), Kabsch (2001) and Pflugrath (1999). In this mode the crystal is rotated by a fraction of its mosaic spread (0.02–0.2°) during each frame, leading to thousands of images for a 180° rotation. Clearly, such an experiment is very time-consuming with a CCD detector. With a fast detector the crystal can be rotated continuously in the beam without opening and closing the shutter for each frame and waiting for the associated additional spindle movement. The readout time of the detector needs to be short in order to reduce the dead-time during the rotation of the crystal. However, this is not a critical parameter for the continuous rotation mode of operation because we need only to reconstruct the finely sampled rocking curve of the crystal. Dead-time does not compromise the data, but does increase the radiation dose on the crystal. And, most importantly, the detector should not add any noise to the data during read out.[1]

We have successfully collected several datasets in fine-φ-slicing mode. It turns out that the analysis of such data with the currently available processing software is not easily done. Therefore we have also collected conventional datasets with normal shutter operation to test the performance of the detector.

This paper is an overview of the PILATUS 1M detector development over the last few years, starting with the description of the readout chip, which is the core component of the detector. The second section is devoted to charge collection of silicon detectors, a very important aspect of single photon counting detectors. Then the fabrication of the modules and the complete PILATUS 1M detector are described. The last section focuses on measurements with the detector in the fall of 2004, where the diffraction patterns of thaumatin, as well as other proteins, were recorded and processed. The measurements and the implementation of the necessary corrections led to the first electron density map ever obtained with a silicon pixel detector.

[1] In an analog system, *e.g.* in a CCD, the readout sequence itself adds noise to the recorded data.

2. The PILATUS I chip

The PILATUS I readout chip was designed in the fall of 2000 at the Paul Scherrer Institute (PSI) and fabricated in the DMILL radiation tolerant CMOS process (Atmel Temic SA, Nantes, France). 6" wafers consisting of 66 chips were available in May 2001. Each chip contains an array of 44 × 78 pixels, with a pixel size of 0.217 mm × 0.217 mm. The pixel chip operates in single photon counting mode at room temperature (*cf.* Llopart *et al.*, 2002). The architecture of the chip is shown in Fig. 1. The chip periphery contains an input/output part, a row selection shift register and column control logic with the column selection shift register. The chip is addressed by setting the signal CHSEL to logic high state. This is necessary for the operation of a chip on a multichip module. Each pixel of the chip can be addressed with the row and column shift registers for programming, readout and diagnostics [*Rowsel* ⊗ (logical and) *Colsel* results in the *Pixsel* signal].

The analog front-end of the pixel cell (Fig. 1, bottom part) is composed of a low-noise charge-sensitive amplifier and a comparator with individual threshold adjustment (Broennimann *et al.*, 2001). The amplifier output of each pixel can be multiplexed onto the analog-out bus of the column and from there to the analog output of the chip. This allows the amplifier noise of each pixel to be measured by selecting the pixel and looking at its analog-out signal, a very useful diagnostic. A calibration signal CAL can be sent to the pixel and the response of the amplifier can be directly seen on the AOUT

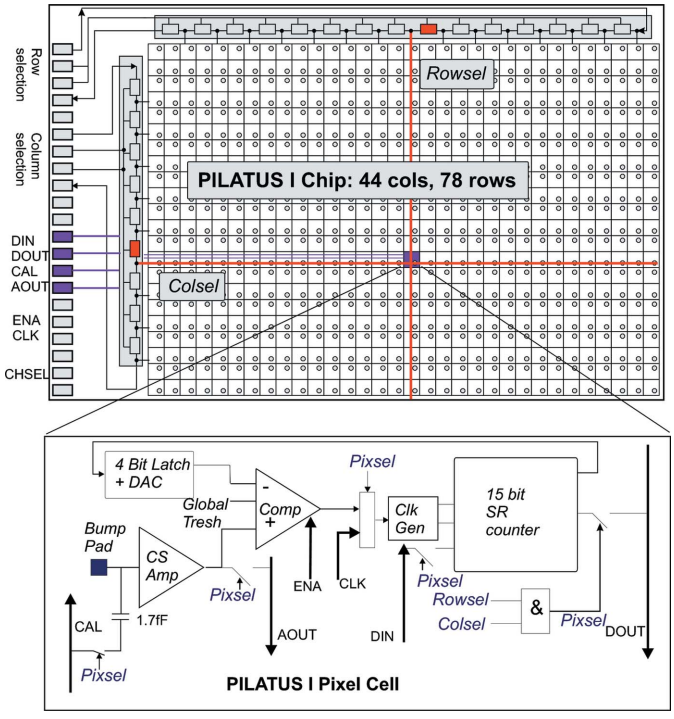

Figure 1
Schematic view of the architecture of the PILATUS I chip (top) with a zoom to a single pixel (bottom). CS Amp = charge-sensitive amplifier; SR counter = shift-register counter. For explanations of other symbols see text.

pad. The r.m.s. noise of a bump-bonded system, measured with an ^{55}Fe source, is 75 e^-, corresponding to a resolution of 630 eV full width at half-maximum (FWHM). The total power consumption is 100 μW pixel^{-1} (0.35 W chip^{-1}). The comparator is AC-coupled to the shaper output and biased by a diode feedback (Broennimann *et al.*, 2001). The intention of the design was to have a low threshold dispersion of the chip. To further reduce the threshold dispersion, each pixel has a 4-bit digital-to-analog converter (DAC), the output of which is added to the global threshold level. The DAC is programmed *via* the DIN pad and selected bits of the 15-bit shift register. A detailed description of the so-called threshold trimming procedure is given by Eikenberry *et al.* (2003). The lowest achievable threshold of the chip is ∼3 keV, which permits ^{22}Ti *Kα* radiation (4.5 keV) to be measured with the detector. The digital part of the pixel consists of a two-phase clock generator, a 15-bit pseudo-random counter and its control logic (Fischer, 1996). The output of the comparator stimulates the clock generator which causes the counter to increment by one.

In count mode, no pixel is selected and the external enable signal ENA acts as an electronic shutter. All the pixels count incoming X-rays in parallel until the ENA signal is set to low. Readout mode is defined by selecting a pixel *via* the column and row shift registers. The external CLK signal is directed to the selected pixel and used as input for the clock generator. The bit content of the selected pixel appears serially at the DOUT pad of the chip. The full readout sequence of the chip is thus a sequential selection of each pixel *via* the shift registers and application of the 15 CLK pulses. The clock frequency is 10 MHz, which, allowing for overhead, results in a readout time of 6.7 ms for the complete chip. The *xy* addressing scheme of the pixel allows readout of subsections of the chip with shorter times. The maximum measured clock frequency of the clock generator and the shift register is 33 MHz. However, Poisson-distributed events with average rates above several kHz can lead to faulty values in the counter of a pixel because of a subtle design flaw that allows two X-rays arriving within 300–500 ns to cause miscounting of the shift-register counter. Therefore the measurements with the PILATUS 1M detector are usually carried out at count rates below 10 kHz pixel^{-1}.

3. Charge collection and charge sharing

The sharing of signal charge between neighboring pixel cells needs to be investigated for single photon counting detectors since if an X-ray is converted at the boundary between two pixels the signal charge might be spread over two (or more) pixels and trigger them. In such a case one X-ray is counted twice (Broennimann *et al.*, 2000, 2002). In order to quantify this effect the charge collection behavior of a bump-bonded PILATUS I assembly was characterized in detail. This study makes use of the special feature of the PILATUS I chip that permits direct access to the analog output of each pixel's shaper.

3.1. The sensor

The basic principle of radiation detection with position-sensitive silicon detectors is described in many publications (*e.g.* Lutz, 1997). The silicon pixel sensors used in the PILATUS 1M detector were designed at PSI and fabricated by Colybris SA, Neuchatel, Switzerland. Each pixel consists of a pn-junction realised by a highly doped p-electrode implanted into a high-resistivity (∼8 kΩ cm) n-bulk. In order to obtain a small pixel capacitance and large lateral electric fields (counteracting charge sharing) the size of the p-implant is 110 μm × 110 μm with a pitch of 217 μm × 217 μm. The implants are contacted by aluminium pads through vias in the oxide. The whole sensor is passivated with ∼1 μm-thick SiO_2 opened only at the positions of the bump pads. The back is unstructured and consists of an aluminium layer contacting a high-dose n-implant.

When a positive bias is applied to the back, a depletion region starts to grow from the pn-junctions towards the back. The bias voltage creates a three-dimensional field distribution in the sensor with the field lines originating from the back of the sensor and ending at the p-implant.

Absorbed X-rays generate a number of electron–hole pairs N_{eh} proportional to the X-ray energy E_x, $N_{eh} = E_x/3.6$ eV. The ionized charge carriers move along the field lines and induce an electrical signal on the collecting electrode. In the case of a highly segmented pixel detector with the readout electronics mounted on the p-side of the sensor, most of the signal is induced by the holes in the last part of their drift path. The PILATUS I sensors with a thickness d = 320 μm deplete at a bias voltage $V_b \simeq 30$ V. However, we observe a much improved collection of the charge at $V_b \simeq 100$ V, which is in agreement with the observations of Tlustos *et al.* (2003). For holes with a mobility of $\mu_p = 505$ cm^2 V^{-1} s^{-1}, a drift time of

$$t_d = d^2/(\mu_p V_b) = 20\,\text{ns} \quad (1)$$

is expected. During the drift the cloud of holes is widened due to diffusion. For a charge cloud generated at the back of the sensor, σ of the Gaussian distribution is

$$\sigma_x = \left[2(kT/q)\mu_p t_d\right]^{1/2} = 7.3\,\mu\text{m}, \quad (2)$$

with kT/q = 0.026 V at 300 K (Lutz, 1997).

X-rays which are absorbed in the boundary region between pixels can thus create a signal in more than one pixel; in the worst case the charge is shared between four pixels.

3.2. Measurements with charge injection by a laser

The individual addressing of each pixel and monitoring of its analog output signal allows detailed study of the effect of charge sharing. To inject charge into the sensor a pulsed infrared LED is used which emits at λ = 904 nm, resulting in an absorption length in silicon of 37 μm. The light spot is focused on the sensor *via* an optical fiber and a lens. The housing of the fiber and the lens are mounted on an *xy* stage, and can be moved with micrometer precision relative to the sensor. The sensor is illuminated from the back after locally removing the aluminium layer. The width of the Gaussian-

shaped laser beam is measured by scanning over a metal edge and is

$$\sigma_{\rm L} = 11 \pm 0.8\,\mu{\rm m}. \quad (3)$$

By comparing the analog pulse-response of the injected laser-signal with the response to 6 keV X-rays, the intensity of the light spot can be easily calibrated and was set to 10 keV. The pulses were injected at a rate of 1 kHz, and the analog output of the pixel was measured with an oscilloscope. The amplitudes of 1000 pulses were averaged and recorded. In order to investigate the charge sharing between two pixels, the laser was moved in 5 µm steps from the centre of a pixel to its direct neighbor. The amplitudes of the left pixel $A_{\rm L}(x)$ and of the right pixel $A_{\rm R}(x)$ were determined at each point. The measured amplitudes were then normalized to the amplitudes at the centers of the pixel, $A_{0\rm L}$ and $A_{0\rm R}$,

$$A_{N\rm L}(x) = A_{\rm L}(x)/A_{0\rm L} \quad \text{and} \quad A_{N\rm R}(x) = A_{\rm R}(x)/A_{0\rm R}. \quad (4)$$

Fig. 2 shows the normalized amplitudes $A_{N\rm L}(x)$ and $A_{N\rm R}(x)$ as a function of the position on the sensor. As expected, the 50% levels of the two curves cross exactly at the boundary between the pixels. At this position the charge generated by an X-ray or the laser is shared between two pixels. The derivatives of the two curves are Gaussians, with

$$\sigma_{\rm tot} = 15.8 \pm 1\,\mu{\rm m}. \quad (5)$$

Subtracting the contribution from the laser, (3), leads to the measured spread of the collected charge,

$$\sigma_{\rm c} = \left(\sigma_{\rm tot}^2 - \sigma_{\rm L}^2\right)^{1/2} = 11.3 \pm 1.3\,\mu{\rm m}, \quad (6)$$

which is somewhat higher than expected from (2). The reason for this discrepancy is unclear.

In order to obtain a two-dimensional picture of the charge collection, the laser diode was moved in x and y over the pixel. The xy position of the laser was recorded if the analog output of the pixel was exactly 50% of the amplitude $A_{0\rm L}$ at the center of the pixel. The resulting plot is shown in Fig. 3. The effective area $A_{\rm eff}$, in which more than 50% of the charge was collected, was measured to be

$$A_{\rm eff} = 92.5\% \quad (7)$$

of the total pixel area. This value, which depends on pixel size and sensor thickness, represents the fact that the charge cloud generated at the boundaries along the pixel is shared between the neighboring pixels.

If the threshold th of the comparator is set to

$${\rm th}_0 = E_x/2, \quad (8)$$

only X-rays within the effective area $A_{\rm eff}$ are counted. If the threshold is lower than $\rm th_0$, some X-rays converting close to the pixel boundaries are counted in both pixels. On the contrary, if the threshold is higher than $\rm th_0$, the count rate is reduced, because in some cases the partial charge does not exceed the threshold. The effect of the threshold setting on the count rate is illustrated in Fig. 4, where the average count rate of 10 pixels stimulated with 12 keV X-rays is shown.

The slope of the count rate is fitted, and then normalized to the count rate at $\rm th_0$. The resulting dependence of the count rate to the threshold setting, in $\rm e^-$, is

$$c_{\rm s} = -9.0 \pm 0.8\%/1000\,{\rm e}^- \quad (9)$$

around $\rm th_0$. For single photon counting detectors it is thus important to adjust the threshold in each pixel as precisely as possible to $\rm th_0$.

It should be mentioned that in a few sensors we observe pixels with reduced charge collection area, $A_{\rm eff}$. This was noticed when such a sensor was illuminated homogeneously with X-rays. Pixels in regions close to the chip edges show a count rate which is reduced by 20%. Such pixels were inves-

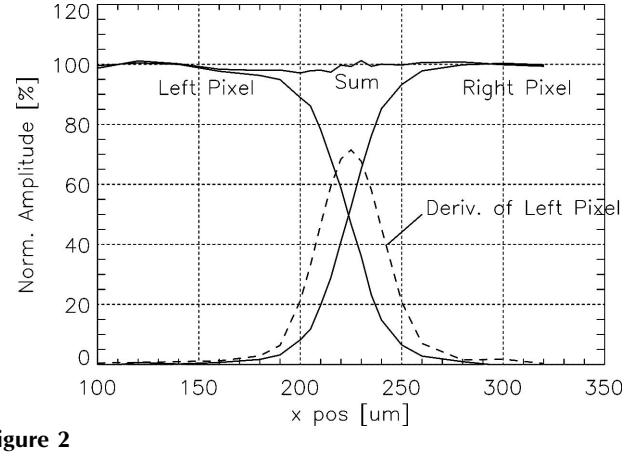

Figure 2
Result of a linear scan with the laser diode over the boundary of two pixels. The normalized amplitudes $A_{N\rm L}(x)$ and $A_{N\rm R}(x)$ as defined in (4) are plotted as a function of the position on the sensor. The dashed line is the derivative of $A_{N\rm L}(x)$, which was fitted with a Gaussian (not shown).

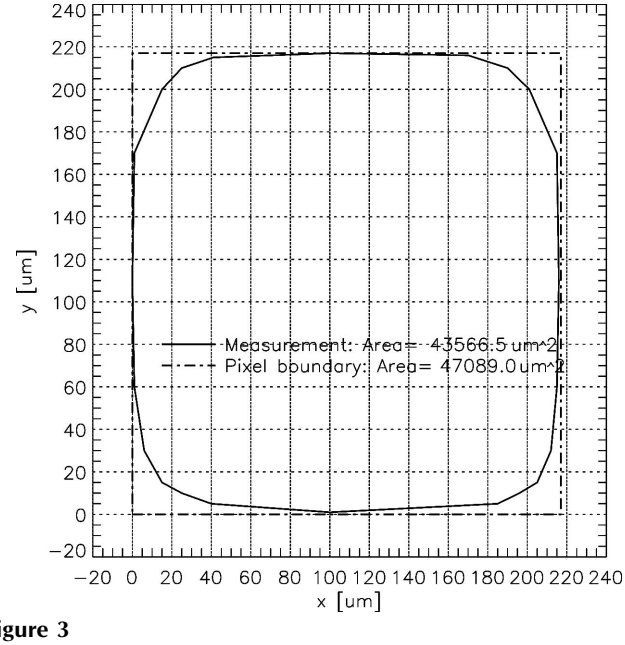

Figure 3
xy scan with the laser diode at the position with 50% of total charge. The resulting effective area, from which more than 50% of the total charge is collected, is indicated. This corresponds to an effective charge collection area of 92.5% of the pixel.

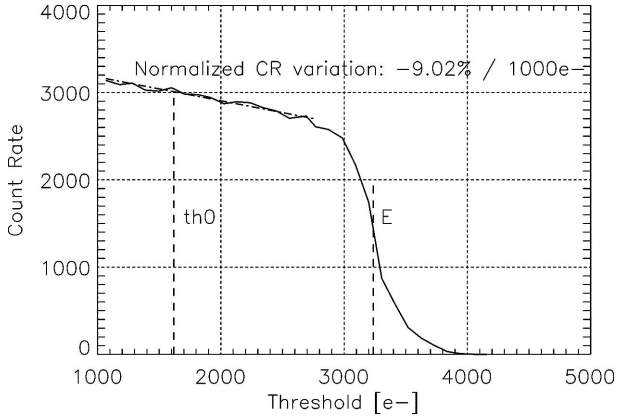

Figure 4
Results from illumination of a sensor with 12 keV (3330 e^-) X-rays. The average rate in ten pixels is plotted as a function of the comparator level in e^-. Below 10 keV (2800 e^-) a straight line is fitted to the data (dash-dotted line).

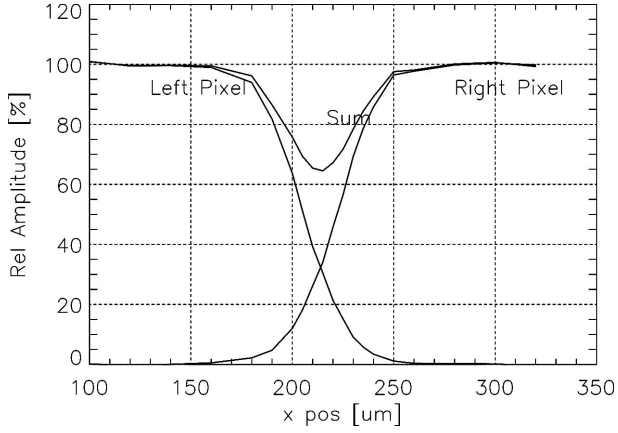

Figure 5
Identical measurement as in Fig. 2 but of pixels which show reduced charge collection area.

tigated with the laser set-up as described above. Fig. 5 shows the normalized amplitudes as defined in (4). The resulting charge collection area is $A_{\rm eff}$ = 77%, which agrees with the measured count rates per pixel. It appears that the charge collection efficiency is influenced by the humidity of the ambient air, perhaps by a thin film of water on the sensor. Keeping the sensors at an elevated temperature of 50°C in dry air led again to a 'normal' behavior for a certain period. The mechanism responsible for the charge loss, however, is not understood.

The correction for the described effects is performed in two steps. In the first step, a threshold adjustment procedure is carried out, to adjust the thresholds of each pixel to $\rm th_0$ as defined in (8). This will still leave the pixels with a distribution of $\sigma_{\rm th_0}$ resulting in count-rate variations that can be calculated by using (9) as described by Eikenberry *et al.* (2003). Then, the pixels need to be illuminated homogeneously with X-rays (flat-field illumination, see Huelsen, 2005) to record the count rates of each pixel, resulting in an image of count rates $A(i,j)$ of each pixel (i,j). In the simplest case (detector far away from the source) the correction factors $F(i,j)$ can be found *via*

Table 1
Physical layout of the multichip sensor.

In order to span the gaps between chips, special pixels are inserted. The sensor is continuously sensitive.

	x	*y*	Total
Pixels per chip	44	78	3432
Chips per module	8	2	16
Bumps per module	352	156	54912
Columns and rows inserted between chips on module	14	1	
Pixel array of module	366	157	57462
Regular pixels per module	338	155	52390
Double wide pixels (344 μm × 172 μm)	14	155	2170
Double high pixels (172 μm × 344 μm)	338	1	338
Edge pixels (344 μm × 344 μm)	14	1	14

$$F(i,j) = I_{\rm max}/A(i,j). \quad (10)$$

$I_{\rm max}$ refers to the maximum of the array $A(i,j)$; the choice of $I_{\rm max}$ as normalization factor is arbitrary. $F(i,j)$ is then applied to each subsequent image and will account for the remaining threshold variations and the variations of the charge collection area $A_{\rm eff}$.

In summary, charge sharing is an important property of thick solid-state digital pixel detectors which has the potential to distort the recorded data. However, its effects can be quantified, and compensated by appropriate choice of settings and calibration procedures.

4. The module

The fundamental unit of the detector is the module, consisting of a single fully depleted monolithic silicon sensor (Colybris SA) with an 8 × 2 array of readout chips bump-bonded to it. Each sensor is a continuous array of 366 × 157 = 57467 pixels without dead areas. Double-sized pixels are used at the chip boundaries in the horizontal direction and an additional row of pixels in the vertical direction is used to span the gap between readout chips (Table 1). The module covers an active area of 79.42 mm × 34.07 mm. The active area is surrounded by several guard rings, the inner guard is contacted to ground *via* bump bonds on the chip. The guard ring region has a width of 700 μm, leading to a total module area of 80.82 mm × 35.47 mm. The ratio of active/total sensor area is 94.4%.

The sensors are fabricated on 4" wafers, and are delivered with an under-bump metallization (UBM), consisting of a thin layer of TiW/Au on all the pad openings. Complete wafers are delivered to PSI for further processing. After cleaning the wafers, a photolithography step is performed which leaves each pad on the sensor with an opening in the applied photoresist layer. A thin layer of indium is then applied to the wafers *via* vacuum deposition. In a lift-off step, the photoresist is removed from the sensor, leaving each pad with an octagon-shaped indium 'cake', with a thickness of several micrometers. Then the wafers are diced and the modules are cleaned, inspected and stored under nitrogen atmosphere. Now the sensors are ready for the actual bump-bonding process.

The CMOS chips are fabricated on 6" wafers. They are cleaned and a photolithography step similar to the one on the sensor wafer is performed, leaving an opening in the photo-

resist on the pad of each pixel. With magnetron sputtering, a thin UBM layer of Ti/Ni/Au is deposited on the pads, followed by indium evaporation. The photoresist is removed from the wafers and they are diced. Now the diced chips are sticking on blue tape, still precisely aligned with respect to their original positions. All the chips are electrically tested on a manual probe station. The yield of 'good' chips is about 35%, but even good chips still have around 160 defective pixels (4.7%). The accepted chips are then cleaned and stored. The components for a module, namely one sensor with indium cakes and 16 chips with UBM and indium deposition, are ready for bump-bonding.

The thin indium cakes on the sensor form into spheres after reflowing the sensor in a reactive gas atmosphere at 453 K (the melting point of indium is 427 K). The indium bumps have a diameter of $\sim$18 µm after the reflow. Each chip is precisely positioned and pressed on the sensor with a force of about 1 g bump^{-1}, which squeezes the indium bumps to about 5–10 µm. After placing all the 16 chips, the complete assembly undergoes a second reflow process, during which the chip–sensor distance increases to $\sim$15 µm. This process aligns the chip with a precision of $\sim$1 µm with respect to the sensor.

In order to test the bare bump-bonded module, three evaluations are carried out:

(i) A pull test on each chip with a force of 75 g. A well bonded chip holds >500 g. If a chip is pulled off it can be replaced by another chip, since all the indium remains on the sensor. After re-bonding and a second reflow, the chip is mated well with the sensor.

(ii) Optical measurement of reference points on the chips to determine chip-to-chip distances. Misaligned chips are identified, pulled off and replaced.

(iii) Electrical test of the chips of the bare Si modules with a probe station. In some cases we observed that chips are destroyed during the bump-bonding process. Towards the end of the fabrication phase we were able to pull off such chips from the sensor and replace them with so-called rework chips.

The bare Si module is glued to a 0.3 mm-thick silicon baseplate for mechanical stabilization. This assembly is then glued onto the readout board and wire-bonded. A single module assembly is shown in Fig. 6.

The module control board (MCB) shown in Fig. 6 is a 6/2 layer Dycostrate flex print (DYCONEX, Advanced Circuit Technology, Bassersdorf, Switzerland). It contains an array of optocouplers to provide electrical isolation of all incoming and outgoing signals. All the regulators for the supply voltages of the chips and the DACs for the biasing of the amplifiers are on the board. An I^{2}C serial interface is used to control the DACs. The comparator level can be programmed for each chip individually, while all the other bias voltages are globally distributed to the 16 chips. Each chip can be individually addressed *via* the I^{2}C serial interface. This is important for the threshold trimming of the pixels and for debugging purposes. It allows accessing each pixel of the module to program its trimbits, to send a calibration pulse or to look at its analog output. However, during normal operation all the necessary steering signals for the chips are applied in parallel. The global

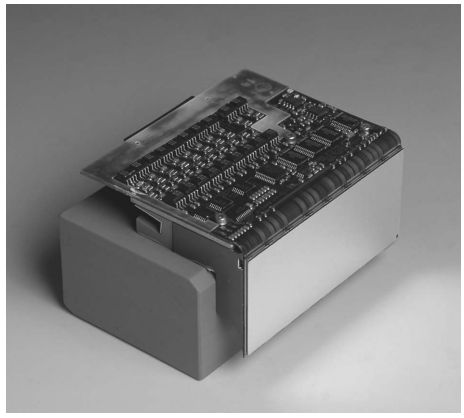

Figure 6
Single module assembly with 8 × 2 chips, mounted on the flex print circuit. The silicon sensor is the vertically oriented plate, viewed from the unstructured aluminized side. The flex print constitutes the Module Control Board (MCB), with the electronic components to operate the 8 × 2 chips. The edges of the eight chips in the upper row can be seen at the edge of the sensor. These are wire-bonded to the curved flexible circuit.

ENA signal defines the exposure time of all the chips. The readout signals to address the shift register, the DIN and DCLK signals (§2) are all applied in parallel to the 16 chips. Each chip has an individual DOUT line on the MCB which is then transmitted *via* the optocouplers. The readout sequence is applied at a clock frequency of 10 MHz, which leads to a readout time of 6.7 ms for the module.

The quality of the bump-bonds in the fabricated module is examined in the following way. First, an image $\mathrm{Im}_0(i,j)$ ($0 < i < 366$, $0 < j < 157$) is taken by applying 100 calibration pulses to each chip (Fig. 7*a*). The pixels counting less than 50 ($\sim$5% of the pixels) are marked with 1 whereas the good pixels are marked with 0 in a binary mask $B(i,j)$. The pixels marked with 1 in $B(i,j)$ have a problem in the readout chip, which is unrelated to the bump bonding. An ^{55}Fe source is placed on four predefined positions over the module and a 100 s exposure is performed at each position. The four images are added to form $\mathrm{Im}_x(i,j)$ (Fig. 7*b*); the intensity is such that the good pixels have more than 50 counts in Im_x. By adding the bad pixel map a new image is created, $\mathrm{Im}_1(i,j) = \mathrm{Im}_x(i,j) + 100\,B(i,j)$. The pixels having below 20 counts in $\mathrm{Im}_1(i,j)$ are regarded as missing bump bonds. $\mathrm{Im}_1(i,j)$ is shown in Fig. 7(*c*). The number of missing bump bonds of ten modules determined with the above procedure is less than about 30 bumps per module. One module has 16 × 3432 bumps = 54912 bumps, which thus leads to 0.05% bad bumps.

5. The detector system

In Fig. 8 the front and back views of the PILATUS 1M detector are shown. Three modules in a row form one so-called bank. The banks are tilted by $\sim$6° with respect to the mounting frame and the modules overlap in the vertical direction in order to reduce the dead area. Optical metrology on the full detector was used to determine the position and orientation of each module with micrometer precision. The standard deviation of the average module position is

Table 2
Parameters of the PILATUS 1M detector system.

Detector type	Array of 18 hybrid-pixel modules
Sensor	0.3 mm-thick Si pn-diode array
Active area	243 mm × 210 mm
Number of pixels	1120 × 967; 1.1 million
Pixel size	0.217 mm × 0.217 mm
DQE at 12 keV	75%
Readout time	6.7 ms
Frame rate	10 Hz
Energy range	$E_{\text{X-rays}} > 4$ keV
Counter	15 bit

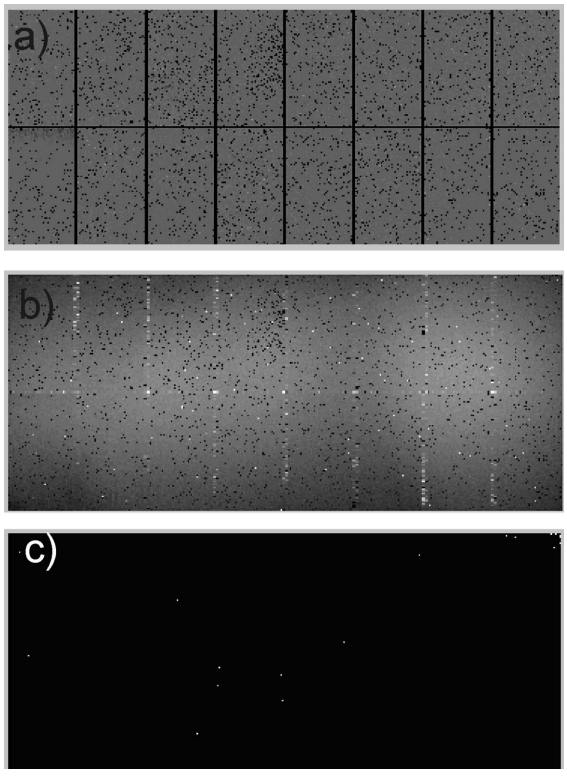

Figure 7
Response of a single module to (*a*) 100 calibration pulses and (*b*) to illumination with an ^{55}Fe source. In (*c*) the resulting bad bump map as explained in the text is shown.

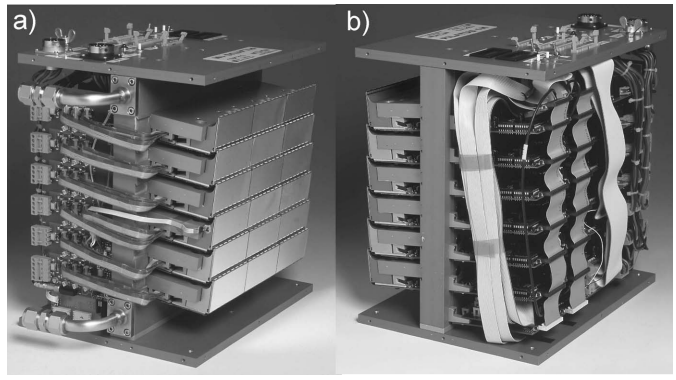

Figure 8
(*a*) Front view and (*b*) back view of the PILATUS 1M detector. On the front the panel of 18 modules is clearly visible. The horizontal row of three modules is designated as one bank; the detector consists of six banks. The banks are tilted by 6° to overlap the modules vertically. On the back, seven PCB boards are visible. The lowest is the so-called detector control board (DCB) and above it are the six so-called bank control boards (BCBs). They are connected *via* two parallel 50-pin cables.

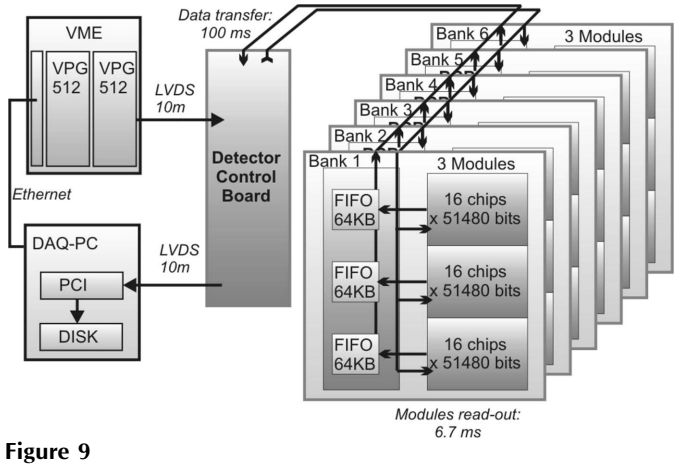

Figure 9
Block diagram of the readout architecture of the detector (see text).

~300 µm. The technical parameters of the PILATUS 1M detector are listed in Table 2.

The detector supply is subdivided into the power for the 18 modules (7 V, 27 A) and the power for the digital readout system (5 V, 15 A); the total power dissipation of the detector is 250 W. The mechanical frame, which holds the modules, is water cooled to 291 K; the sensor surfaces have a temperature of ~300 K. The detector is packed into a box with a 20 µm-thick aluminized mylar foil as entrance window. The detector box is flushed with N_2, to achieve a relative humidity below 10%.

The readout architecture is shown in Fig. 9. Each bank is electrically serviced by a bank control board (BCB). Steering signals for the detector are supplied from two VPG512 VME pattern generators (40 MHz, 16-bit, Dipl. Ing. Kramert AG, Remigen, Switzerland). All the steering signals are converted in one detector control board (DCB) to 3.3 V TTL and from there distributed to the six BCBs. The readout of all the modules is carried out in parallel within 6.7 ms and the digital data are then stored in Cypress 64k FIFOs on the BCBs. While all the modules are re-enabled for counting, the data are serially transmitted from the FIFOs to the data acquisition card (DAQ) card (PCI10k-PRODB by PLD Applications, Aix-en-Provence, France) residing in a PCI^2-bus slot of the DAQ computer. This minimizes the dead-time of the chip, and permits the necessary data transfer to disk during the next exposure time. The architecture implements an addressing scheme bank–module–chip–pixel, which allows selection of an individual pixel within the array. This allows programming of the 4-bit DACs in a pixel for the threshold fine tuning and examination of its analog output signal for calibration and debugging purposes.

The threshold trim adjustment procedure with a target threshold of 6 keV takes about 15 min (Eikenberry *et al.*, 2003). The resulting threshold setting of all the pixels within the detector is 6 ± 0.2 keV (see Fig. 10).

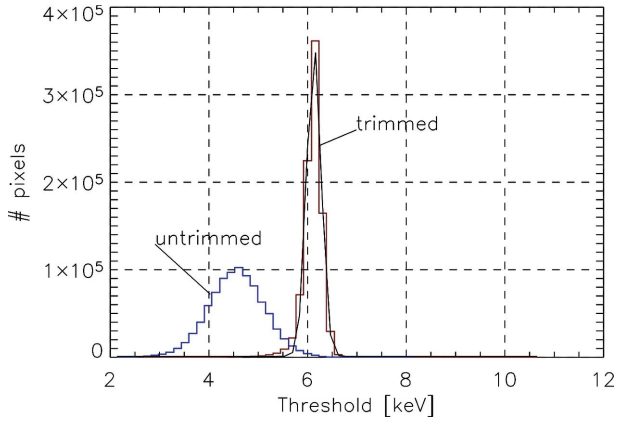

Figure 10
Threshold distribution of all the pixels with and without threshold trimming. The solid line is a Gaussian fitted to the data. The r.m.s. of the trimmed threshold distribution is 0.2 keV (55 e^-); that of the untrimmed distribution is 0.7 keV.

The PILATUS 1M detector constitutes a 1120 × 967 pixel array. The number of dead pixels within the active area is comprised of the following:

(i) Pixel bump-bonding defects: the average number of unconnected pixels in good modules is 0.05%. However, there are two modules in the array which are worse, resulting in an overall bump-bond yield within the detector of 98.8%.

(ii) Pixel defects in the readout chips: this is a problem of the DMILL process; 4.7% of the pixels on a chip have analog or digital defects after wafer level screening and selection.

(iii) Chip defects, ten out of the 288 chips are not responding (3.2%): five chips in one module are from a badly processed wafer, two were destroyed during wire-bonding and three were destroyed during the bump-bonding process. At the end of the fabrication phase, three other defect chips on modules were replaced by a rework procedure.

(iv) Gaps between modules: five pixels in the vertical direction and 11 pixels in the horizontal direction, total 48422 pixels (4.4%).

(v) Shadow from the overlap of the modules at 1 m distance, detector center at beam height: 25000 pixels (2.3%)

In total, 15.9% of pixels do not respond to X-rays. To overcome this drawback, the detector is mounted on a precision translation stage. Since no readout noise is added to the data by the detector, crystallographic data is usually collected twice with the detector shifted between datasets.

6. Protein crystallography with the PILATUS 1M detector

Recording and processing of crystallographic data with the PILATUS 1M is different from data collection with commercial CCD detectors. First, the treatment of the dead pixels requires special attention. Typically, Bragg reflections with signals in one of the eight neighbors of a dead pixel will be rejected. Thus, the class (i) and (ii) defects as described in the previous section have a much stronger influence on the completeness of the data than the dead areas between the modules. A second difficulty arises from the geometrical arrangement of the modules. Smooth distortion functions are applied to fiber-optic taper CCD detectors. The pixel detector consists of 18 individual modules that each have three degrees of positional and two degrees of rotational freedom. The average tilt angle of 5.83 ± 0.08° leads to geometrical corrections that are dependent on the sample–detector distances. Therefore, specific correction files need to be calculated for the actual position of the detector at the beamline. A third point of attention is the actual count rate per pixel and the exposure time. The rate per pixel has to be limited to ∼10 kHz, and the exposure time needs to be adapted in such a way that strong reflections do not cause pixels to record more than ∼15000 counts, although the maximum count number is 32767. Overflow must be avoided because the counter restarts at 1, which is impossible to correct by software in the presence of the ambiguity introduced by miscounting (above). The fourth difference from CCD data arises from the amount of data produced by the fine-φ-slicing mode. In these experiments the angular velocity of the diffractometer is set to a fraction of the mosaicity of the crystal, yielding thousands of images for a full dataset.

Several days of beam time were allocated at the protein crystallography beamline X06SA during 2004. Multiple redundant datasets from single crystals of the proteins lysozyme, thaumatin, GapN and insulin have been collected with PILATUS 1M. Conventional shutter-operated data were recorded as well as fine-φ-sliced data with continuous rotation of the sample and no shutter operation. Data were recorded under low-, medium- and high-intensity beam conditions. The procedure for one dataset is described in the following.

The DAC values with the target threshold setting of 6 keV were downloaded to each pixel. The beam was adjusted to 13.5 keV and flat-field data were collected with bromine fluorescence X-rays (11.9 keV) from a KBr sample. For this purpose the detector was positioned at 90° with respect to the beam and the flat-field data were collected at the distance corresponding to the crystal-to-detector distance used for the data collection (d = 128 mm). Correction factors $F(i,j)$ similar to (10) were calculated.

The detector was positioned on the A-frame of beamline X06SA (Fig. 11). The energy was set to 12 keV and a thaumatin crystal, cryocooled in a rayon loop, was mounted. After evaluating some single test images, the beam intensity was attenuated to 13.5%. The integration time was set to 4 s and the rotation was 1° per image. A 120° dataset of images, D_{1k}, was acquired, with $0 \leq k < 120$ at position 1. Now the detector was translated with micrometer precision by 217 µm (one pixel) in the horizontal direction to position 2 and a 120° dataset, D_{2k}, was acquired; for the third dataset, D_{3k}, the position was again shifted by one pixel. The images of the three datasets were then individually multiplied by $F(i,j)$, *i.e.* flat-field corrected, and all the unreliable pixels were blanked out. The non-zero data for each pixel in the three datasets were averaged.

On the resulting dataset, D_k, the distortion correction procedure was applied, which is described in detail by Huelsen

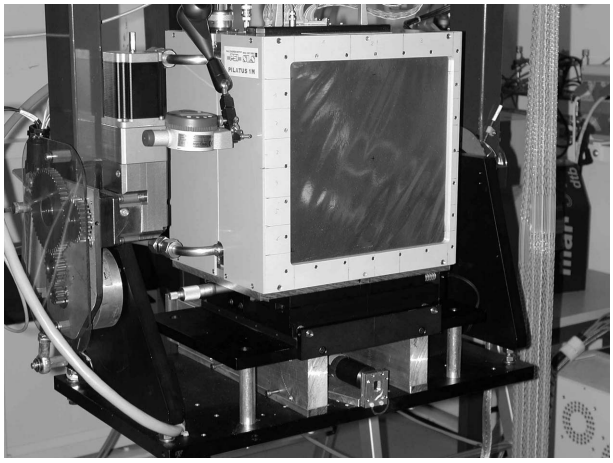

Figure 11
The PILATUS 1M detector at beamline X06SA.

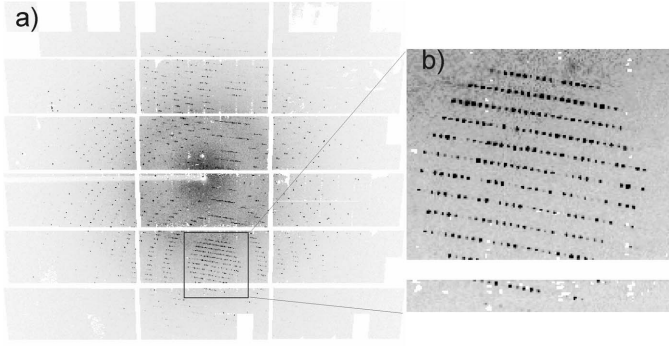

Figure 12
(a) One of 180 corrected frames with 4 s exposure and 0.5° rotation from a thaumatin crystal. (*b*) Zoom of a selected region. The resolution at the edge of the detector is 1.4 Å.

et al. (2005) and is briefly summarized here. First the module displacement is considered and each pixel is corrected by the exact module position in space. Now the angle of incidence of the X-rays from the sample onto each pixel is calculated. A parallax back-transformation is carried out. The data now represent the impact point of the X-rays on the sensor surface. The last step is the projection of the data from the 6° tilted sensor surfaces to a virtual flat plane at the front of the detector.

In order to verify the geometrical correction algorithm, images of a precision hole-mask were recorded. The 0.2 mm-thick Ta mask contains a 45 × 40 array of holes of diameter 0.2 mm with 5 mm spacing (∼100 holes per module). The mask was placed ∼3 cm in front of the sensor surface and the detector was illuminated with monoenergetic X-rays from a fluorescent sample. These images were then analysed and the r.m.s. deviation σ_h of the holes from a least-squares-fitted grid was determined. This procedure helps to determine systematic errors of the geometrical correction algorithm. The final algorithm leads to an r.m.s. deviation from the ideal grid of the measured holes of $\sigma_h < 75$ µm.

After correction of the images D_k ($0 \leq k < 120$), the dataset is ready to be processed with one of the standard crystallographic software packages. A corrected image from the thaumatin data is shown in Fig. 12(*a*), with a zoom-in of a selected region in Fig. 12(*b*).

Table 3
Data-collection parameters and figures of merit from a thaumatin dataset and its refinement.

The numbers in parentheses refer to the highest resolution shell (1.5–1.4 Å). R_{int} is the internal *R*-factor obtained from *XDS* (Kabsch, 1993). R_{cryst} is the result of the refinement of the data by *SHELXL* (Sheldrick & Schneider, 1997).

Space group	$P4_12_12$
Cell constants (Å)	$a = 57.78$; $c = 150.7$
Wavelength (Å)	1.04
Oscillation range (°)	1.0
Exposure time (s)	4.0
Crystal–detector distance (mm)	128
Mosaicity (°)	0.1
Total number of reflections	352535
Number of unique reflections	86141
Resolution range (Å)	10–1.4
Completeness (%)	90.3 (60.5)
$\langle I/\sigma(I)\rangle$	10.3 (3.9)
R_{int} (%)	8.4 (26.4)
R_{cryst} (%); working set	20.0
R_{cryst} (%); free set	22.9

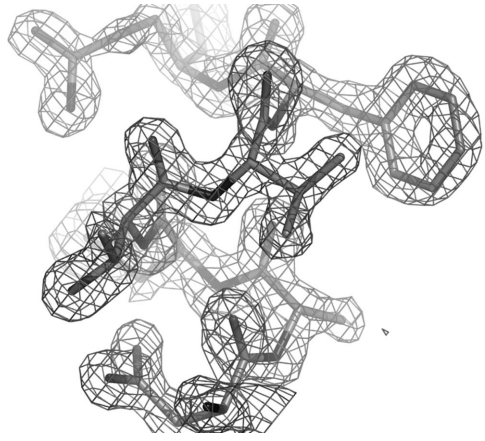

Figure 13
A section of the electron density map of thaumatin after the refinement ($2F_o - F_c$, 2σ contour level). The electron density is of good quality and shows all features expected at 1.4 Å resolution.

Table 3 summarizes the statistics from a conventional experiment and figures of merit from the data processing with the program package *XDS* (Kabsch, 1993). The structure was solved by molecular replacement using a structure model solved by *S-SAD* at beamline X06SA (Wagner, 2005). The subsequent isotropic refinement of the thaumatin structure against the measured diffraction data with *SHELXL* (Sheldrick & Schneider, 1997) led to reasonable statistics (also in Table 3). Fig. 13 shows a section of the electron density map after the refinement ($2F_o - F_c$, 2σ contour level; F_o are the observed, F_c are the calculated structure factors). The electron density is of good quality and shows all the features expected at 1.4 Å resolution.

The short readout time of the PILATUS 1M detector allows the collection of crystallographic data without any shutter operation and with very high angular resolution. For this

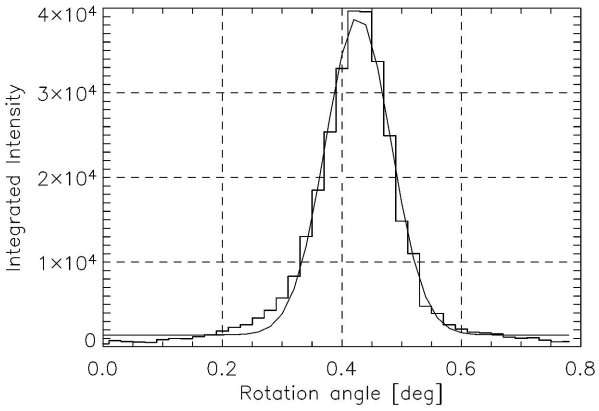

Figure 14
Rocking curve of a representative reflection from the 9000 frames ($\Delta\varphi$ = 0.02°) of an insulin dataset. The solid line is a Gaussian fitted to the curve with a FWHM of 0.13°.

experiment the angular velocity of the diffractometer was set to 0.02° s^{-1} and the integration time of the detector was set to 1 s. The shutter was opened, the crystal rotated with the preset angular speed and the detector was operated in a continuous loop mode with the preset exposure time followed by the 6.7 ms readout cycle. The detector timing is implemented in hardware based on the 40 MHz clock of the VPG512. The crystal was rotated by 180° and 9000 frames were acquired. The high angular resolution leads to higher precision of each recorded reflection (Pflugrath, 1999). The analysis of the fine-φ-sliced datasets with *XDS* is ongoing.

A rocking curve of one reflection is shown in Fig. 14. The mosaicity of this crystal is about 0.13°. By setting the angular velocity of the diffractometer to a fraction of the mosaic spread of the crystal per exposure, each Bragg spot stays in the full reflection condition for several images and thus can deliver a very high rate to the target pixel. This can cause counter overflows or miscounts, as mentioned in the first section. Typically the beam intensity is reduced by a factor of more than ten compared with a conventional dataset to prevent overflows. In the absence of overflows the over-sampling of the rocking curves helps to overcome the miscounting problem of the detector: each reflection is fitted with a reference profile in φ-space and software then attempts to restore corrupted values. Whether this is helpful in a full fine-slice dataset is under investigation.

7. Conclusions and outlook

The PILATUS 1M detector constitutes the first large-area pixel detector operated at a synchrotron. In many experiments we have demonstrated that single photon counting potentially provides data of superior quality. The charge sharing in silicon detectors can be measured and with an appropriate calibration procedure it appears to have little impact on the experimental data. We have acquired crystallographic data from several test proteins with the detector. During the processing of the data we realised that single dead pixels within the modules are a major problem whereas the dead regions between the modules can be dealt with using appropriate software tools. Data acquisition is therefore carried out at two or more positions, separated by one pixel. This procedure leads to data of sufficient quality to be processed by a standard crystallographic package. The resulting electron density map proves that the data can be analysed if the necessary corrections are applied. Fine-φ-sliced datasets with continuous sample rotation can be collected with the detector owing to its short readout time and the absence of digital noise. These data have a much higher information content than conventional rotation data and will have an impact on the way data are collected in the future. In summary, we have proven for the first time that hybrid pixel detectors can be successfully used for protein crystallography.

Crystallographic data collection with the detector and the results of processing provided very valuable information for the design of the next generation of hybrid pixel detectors. The PILATUS I readout chip will be replaced by a significantly improved readout chip (PILATUS II), fabricated in a 0.25 µm CMOS process. The dynamic range per pixel will be increased to 20 bits (10^6) and the count-rate limit is pushed to 1 MHz, which should allow collection of the full range of the diffracted intensity of a protein crystal in one image. The quality of the chips is much improved and it is expected that there will be no defects in them. Another improvement concerns the geometry of the detector. The geometrical corrections for the 6° tilting of the modules and the overlap can be performed. However, the resulting correction files are position-dependent: for each sample to detector position a new correction file must be calculated, which is not practical for day-to-day usage of the detector at the beamline. We abandoned the tilted arrangement of the modules and we will build the new detector as a flat array of modules. The geometrical corrections will then be much easier to handle and only minor dependence on the actual sample-to-detector position is expected. For the new detector we expect a dead area below 10%.

We would like to thank F. Glaus, M. Horisberger, M. Naef, H. Rickert and S. Streuli of PSI for their help in module fabrication. R. Schneider and C. Pradervand were helping us during set-up and data collection at the SLS protein crystallography beamline X06SA. Many thanks to T. Rohe for his help in the section about charge-sharing and to R. Dinapoli for helping to revise the manuscript. We would like to thank W. Kabsch for valuable discussions and assistance during the processing of the data. GH and AW acknowledge support from the Swiss National Science Foundation and the NCCR Structural Biology, respectively.

References

Boudet, N., Berar, J.-F., Blanquart, L., Breugon, P., Caillot, B., Clemens, J.-C., Koudobine, I., Delpierre, P., Mouget, C., Potheau, R. & Valin, I. (2003). *Nucl. Instrum. Methods Phys. Res. A*, **510**, 41–44.

Broennimann, Ch., Baur, R., Eikenberry, E. F., Fischer, P., Florin, S., Horisberger, R., Lindner, M., Schmitt, B. & Schulze, C. (2002). *Nucl. Instrum. Methods Phys. Res. A*, **477**, 531–535.
Broennimann, Ch., Baur, R., Eikenberry, E. F., Kohout, S., Lindner, M., Schmitt, B. & Horisberger, R. (2001). *Nucl. Instrum. Methods Phys. Res. A*, **465**, 235–239.
Broennimann, Ch., Eikenberry, E. F., Horisberger, R., Hülsen, G., Schmitt, B., Schulze-Briese, C. & Tomizaki, T. (2003). *Nucl. Instrum. Methods Phys. Res. A*, **510**, 24.
Broennimann, Ch., Florin, S., Lindner, M., Schmitt, B. & Schulze-Briese, C. (2000). *J. Synchrotron Rad.* **7**, 301–306.
Eikenberry, E. F., Broennimann, Ch., Hülsen, G., Toyokawa, H., Horisberger, R., Schmitt, B., Schulze-Briese, C. & Tomizaki, T. (2003). *Nucl. Instrum. Methods Phys. Res. A*, **501**, 1–260.
Fischer, P. (1996). *Nucl. Instrum. Methods Phys. Res. A*, **378**, 297–300.
Gemme, C. (2003). *Nucl. Instrum. Methods Phys. Res. A*, **501**, 87–92.
Huelsen, G. (2005). Doctoral thesis, No. 16289, ETH Zurich, Switzerland.
Huelsen, G., Broennimann, Ch. & Eikenberry, E. F. (2005). *Nucl. Instrum. Methods Phys. Res. A*, **548**, 540–554.
Kabsch, W. (2001). *International Tables for Crystallography*, Vol. F., *Crystallography of Biological Macromolecules*, ch. 11.3, edited by M. G. Rossmann and E. Arnold. Dordrecht: Kluwer.
Kabsch, W. (1993). *J. Appl. Cryst.* **26**, 795–800. [Also available at http://www.mpimf-heidelberg.mpg.de/~kabsch/xds.]
Llopart, X., Campbell, M., Dinapoli, R., Segundo, D. S. & Pernigotti, E. (2002). *IEEE Trans. Nucl. Sci.* **49**, 2279.
Lutz, G. (1997). *Semiconductor Radiation Detectors.* Berlin: Springer.
Pflugrath, J. W. (1999). *Acta Cryst.* D**55**, 1718–1725.
Riedler, P., Anelli, G., Antinori, F., Burns, M., Banicz, K., Caliandro, R., Campbell, M., Caselle, M., Chochula, P., Dinapoli, R., Easo, S., Elia, D., Formenti, F., Girone, M., Gys, T. *et al.* (2003). *Nucl. Instrum. Methods Phys. Res. A*, **501**, 111–118.
Schnetzer, S. (2003). *Nucl. Instrum. Methods Phys. Res. A*, **501**, 100–105.
Sheldrick, G. M. & Schneider, T. R. (1997). *Methods Enzymol.* **277**, 319–343.
Tlustos, L., Davidson, D., Campbell, M., Heijne, E. & Mikulec, B. (2003). *Nucl. Instrum. Methods Phys. Res. A*, **509**, 102–108.
Wagner, A. (2005). Private communication.